Article

Comparative Studies of Undoped/Al-Doped/In-Doped ZnO Transparent Conducting Oxide Thin Films in Optoelectronic Applications

Panagiota Koralli [1,*] [iD], Songül Fiat Varol [2] [iD], George Mousdis [1] [iD], Dionysios E. Mouzakis [3,*] [iD], Ziya Merdan [4] and Michael Kompitsas [1]

[1] National Hellenic Research Foundation, 48 Vassileos Constantinou Avenue, 11635 Athens, Greece; gmousdis@eie.gr (G.M.); mcomp@eie.gr (M.K.)
[2] Electric and Energy Department, Vocational School of Technical Sciences, Manisa Celal Bayar University, 45140 Manisa, Turkey; songul.varol@cbu.edu.tr
[3] Hellenic Army Academy, Leoforos Eyelpidon (Varis-Koropiou) Avenue, Vari P.O., 16673 Attica, Greece
[4] Physics Department, Faculty of Arts and Sciences, Gazi University, 06500 Ankara, Turkey; ziyamerdan@gazi.edu.tr
* Correspondence: pkoralli@eie.gr (P.K.); demouzakis@sse.gr (D.E.M.)

Abstract: In this paper, undoped, Al-, and In-doped zinc oxide thin films were deposited. Film growth was performed using the sol–gel technique. The method included (a) preparing homogeneous and stable solutions of zinc acetate 2-hydrate, (b) mixing them with aluminum nitrate and indium acetate in 2-methoxyethanol and 2-aminoethanol solutions with various concentrations, and (c) spin coating them onto transparent glass substrates. After thermal annealing, the films showed a high transparency (80–90%) and good stability. Using typical diagnostic tools, the structural, morphological, optical, and electrical film properties were investigated and linked to the dopant type, and concentrations in view of optoelectronics were investigated.

Keywords: ZnO; Al-doped ZnO; In-doped ZnO; nanomaterials; thin films; sol–gel spin coating; optoelectronics; physical properties; electrical properties

1. Introduction

Transparent conductive metal oxides (TCOs) are very attractive materials, both for research and industry. In general, they provide excellent properties, such as high optical transmittance in the UV-VIS-NIR spectrum and high free-carrier density resulting in good electrical conductivity [1]. In particular, zinc oxide (ZnO) is an n-type transparent semiconductor with a direct wide bandgap of 3.37 eV. Furthermore, it crystallizes in the stable wurtzite structure with a lattice constant of 3.25 Å and has a large exciton binding energy (60 meV). It has been explored in a variety of applications, such as plasma display panels, surface acoustic waves, optical waveguides, flexible displays, photodetectors, and light-emitting diodes (LEDs). To meet the requirements of high-brightness LEDs, the wide-bandgap ZnO semiconductor, with its excellent structural and physical properties, is a better candidate compared to GaN [2]. In addition, ZnO thin films have been used for the development of transparent electrodes for solar cells [3–7], various types of sensors (chemical, bio, and gas) [8,9], thin-film transistors [10], photoconductive detectors [11], and piezoelectric transducers [12]. Furthermore, its salient characteristics are the variety of its synthetic methods, its non-toxicity, and its high stability. Its structure plays an essential role in the determination of a devices' performance (e.g., power conversion efficiency, lifetime, and stability).

ZnO thin films have been grown using various methods, such as spray pyrolysis [13], pulsed laser deposition (PLD) [14], and molecular beam epitaxy (MBE) [15]. Solution-based methods, such as solvothermal/hydrothermal and sol–gel processes, are more attractive

because of the mild synthesis conditions used. In particular, these methods are characterized by low-temperature processing, large substrate area film growth, easy film thickness control, increased homogeneity and purity, efficient microstructural control of metallic particles, high film density and uniformity, and, most importantly, cost effectiveness [7,16,17] for industrial applications.

In fact, ZnO is defined as a savior material as a transparent electrode in Organic Light-Emitting Diode (OLED) applications [18–20]. ZnO/GaN n-p heterojunctions are the most preferred semiconductors for optoelectronic devices. It is well known that the process of producing GaN is very complex. In particular, to produce p-type GaN, doping and activating Mg and keeping the carrier concentration at the desired level (>10^{19}) [21] involve a laborious and costly process such as MOCVD. However, n-type ZnO can be easily produced with the economical sol–gel spin coating technique, which provides high controllability and a straightforward and practical methodology. Therefore, in the production of ZnO/GaN, we can at least achieve ZnO production at a more reasonable cost, making the production of the whole p-n structure more attractive.

In photovoltaic devices, doped indium tin oxide (ITO) and indium zinc oxide (IZO) conductive oxides are mostly preferred due to their high transparency and good conductivity [22]. Sobrado et al. [23] reported the effect of microstructured IZO contacts on amorphous silicon (a-Si) thin-film solar cells. They used a new process to integrate a light-trapping (LT) structure on the front contact of the cells. An enhancement of 26.7% in the cell photocurrent was measured when using an ultra-thin (30 nm) flat IZO layer between the LT structures and the a-Si absorber. Moreover, IZO is used in CIGS solar cells as an antireflector [24]. Jošt et al. [25] presented detailed guidelines on how to achieve high-efficiency tandem devices by using a light-trapping strategy. Textured light management foils added on top of an IZO transparent contact led to a minimization of the light reflection in double-textured monolithic PVSK/Si tandem solar cells and increased energy yield.

The need for increased efficiency of photovoltaic modules has led to the development of two subsequent solar cells of different technologies (tandem structure) in recent years. Kranz et al. [26] combined a large-bandgap (~1.6 eV) perovskite solar cell placed on a small-bandgap (~1 eV) CIGS-type solar cell in a superstrate configuration. As a result, UV and VIS solar photons were efficiently absorbed in the perovskite layer, while the NIR photons were not. The novelty in their work was to replace the typical Au back electrode of the upper cell with a sputtered Al-doped ZnO layer. Therefore, making use of the high AZO transparency, they obtained an NIR-transparent perovskite solar cell, with an average transmission of 71% for photons in the wavelength of 800–1.000 nm. These photons were absorbed by the lower CICS cell, giving altogether an efficiency of 19.5% of the tandem structure, the highest achieved at that time. These results indicate that AZO performs as a better material for the back electrode as well as for the interface between the two cells. More examples from the literature show that the research on ZnO and its doped structures is still attractive today.

In view of sensing applications, ZnO has attracted lots of attention in recent decades. It is one of the mostly used metal oxide materials for gas sensors [27,28]. Although it is sensitive to a variety of volatile and noxious gases, exhibiting good stability, there are still some crucial drawbacks that prevent its expansion in this field. These drawbacks are its high working temperature, low sensitivity, and poor selectivity [29,30]. Many studies have reported different strategies to surmount these disadvantages [31–33]. One of them proposed controllable doping with appropriate metals (Al, In, Ga, Cu, Fe, etc.) to improve ZnO sensing performance. Such dopants, depending on their intrinsic characteristics, as well as their concentration in the film, can amend the structural, morphological, and electro-optical properties by affecting the crystal structure and the development of defects. Among the aforementioned dopants, the group III elements Al and In have been shown to play an important role in improving the performance of ZnO-based sensors. Nimbalkar et al. showed that Al-doped ZnO thin films improved gas sensor response for the detection of NO_2 at a relatively low 200 °C working temperature [28], whilst Bharath et al. presented

a study where In-doped ZnO thin films prepared using spray pyrolysis exhibited a good sensitivity to volatile organic compounds, especially ethanol [34].

In the present work, undoped ZnO, In-doped ZnO (IZO), and Al-doped ZnO (AZO) were prepared on glass substrates using the sol–gel/spin coating method. This series of thin films allowed us to perform an extensive structure–property relationship study by investigating the influence of the dopant type and its concentration on the structural, morphological, and electro-optical properties of the grown thin films. The obtained results provide a clear understanding of how the above-mentioned parameters affected the thin film properties, making them suitable candidates in optoelectronic and sensing applications.

2. Materials and Methods

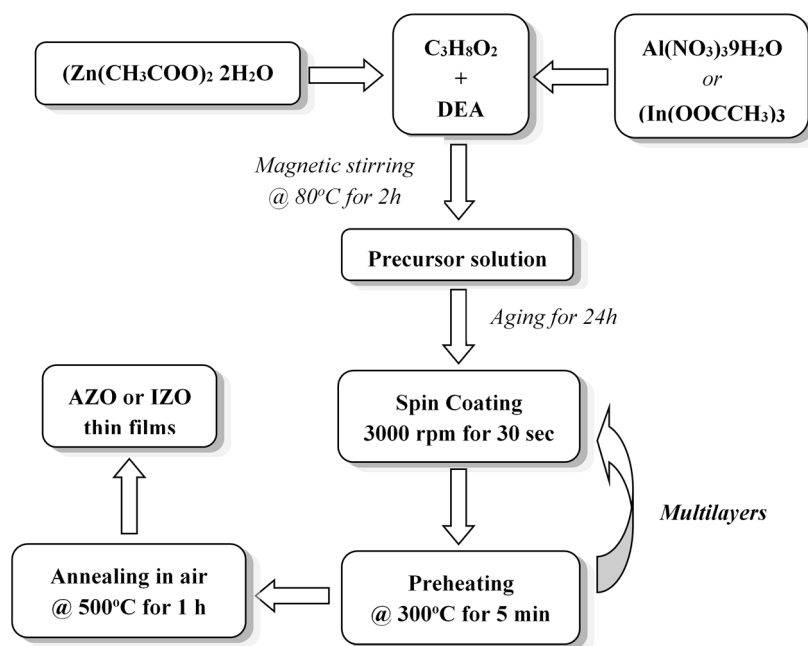The sol–gel spin coating deposition process is schematically given in Figure 1.

Figure 1. Flowchart of sol–gel spin coating deposition process.

2.1. Starting Materials

The precursor solutions for intrinsic, Al-, and In-doped ZnO were prepared using the sol–gel method. Zinc acetate dihydrate ($Zn(CH_3COO)_2$ $2H_2O$, Ferak-01650), aluminum nitrate ($Al(NO_3)_3 9H_2O$, Chem-Lab 00.0121.0250), and indium acetate ($In(OOCCH_3)_3$, Alfa Aesar 42230) were used as precursors, while 2-methoxyethanol ($C_3H_8O_2$) and 2-aminoethanol (DEA) were used as the solvent and the stabilizer, respectively.

Microscope glasses were used as substrates. The substrates were kept in chromosulfuric acid for 24 h for cleaning, then washed thoroughly with distilled water and isopropanol, and finally dried.

2.2. Synthesis

Zinc acetate dihydrate was dissolved in 2-methoxyethanol, and then 2-aminoethanol (DEA) was added slowly under magnetic stirring. The molar ratio of DEA to zinc acetate was maintained at 1.0, while the zinc acetate concentration was 0.5 M. The resultant solution was stirred at 80 °C for 2 h to yield a clear and homogeneous solution, and then it was maintained at room temperature to age for 24 h.

2.3. Film Deposition and Thermal Annealing

Pure or doped ZnO thin films were deposited on glass substrates using the spin coating technique, with a rate of 3000 rpm for 30 s at room temperature. After each coating,

the films were heat-treated at 300 °C for 5 min in air for the solvent and organic residues to evaporate. This procedure was repeated for a number of times, varying from 1 to 10 in order to obtain films with different thicknesses. Finally, these films were annealed in air at 500 °C for 1 h.

2.4. Characterization

X-ray diffraction (XRD) studies were performed using $CuK\alpha_{1,2}$ radiation from a D8 Advance Brucker X-ray generator, operating at 40 mA and 40 kV. Film morphology was examined with a scanning electron microscope (JEOL 6301F microscope) and atomic force microscopy (Dual Scope DS 95-50/200). The AFM images were acquired in contact mode. Optical transmittance spectra were recorded by using a Perkin Elmer Lambda 19 spectrophotometer in the 300–1200 nm range, and the optical bandgap energy was calculated. The resistivity of the thin films was estimated by applying the four-point method, whilst film thickness measurements were performed by profilometry using a KLA-Tencor Alpha-Step IQ surface profiler.

3. Results and Discussion

3.1. Microstructure Analysis

The crystallinity of undoped, Al-, and In-doped ZnO was investigated using XRD. Figure 2a,b show the X-ray diffraction patterns for 2θ values in the range of 20°–75° of pure ZnO and doped ZnO thin films, respectively. All deposited films, regardless of dopants, show diffraction peaks that correlate with the reflection of hexagonal wurtzite-structured ZnO planes. A high intensity (002) peak can be clearly observed, providing strong evidence that the ZnO crystal exhibits a strongly preferred *c*-axis orientation. Several factors influence the orientation of sol–gel ZnO films, such as the parameters of the chemical reactants used (nature and concentration of the precursor, solvent, additive, and solution aging time), the process parameters of the film deposition technique and the choice of substrates, and the pre- and post-heat treatment conditions [35]. The reason for such preferred growth is that, on the one hand, the (002) plane presents the minimum surface energy [36], driving a higher growth rate along the *c*-axis than in other crystallographic orientations, and, on the other hand, this specific orientation is the kinetically preferred one presenting a higher degree of grain packing [37].
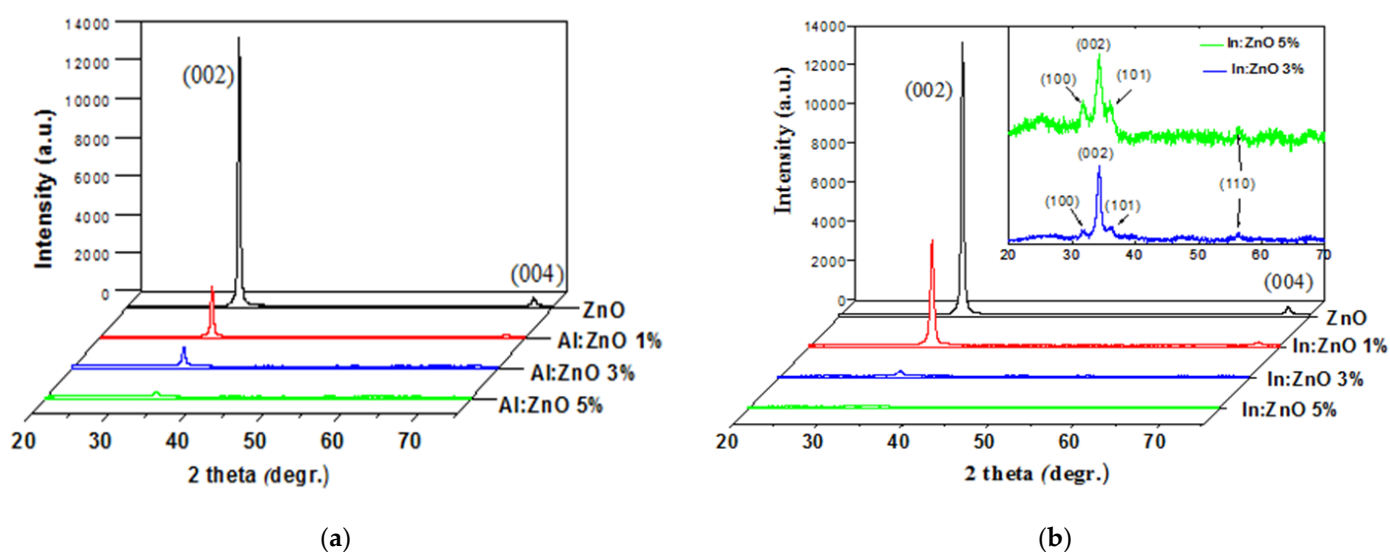

Figure 2. The X-ray diffraction patterns for undoped, AZO (**a**), and IZO (**b**) thin films.

Nevertheless, it is noticed that Al and In doping dramatically influence the film's evolution process. Despite the fact that the majority of the crystals develop along the (002)

direction and only a few crystals grow along other directions, such as the (004) direction for undoped and Al-doped ZnO, the In-doped thin films exhibit crystallization to the additional orientations (101), (100), and (110) for concentrations greater than 1% (see inset in Figure 2b). It is perceived that the induction of amorphous phases is caused due to the competition of Zn^{2+} ions with Al^{3+} and In^{3+} ions in order to capture more O atoms, forming higher Al–O/In-O bonding states. This phase raises the possibility of obstructing crystal growth, affecting the preferential crystalline plane orientation [35]. The absence of (002) and (102) planes may be induced by the crystalline distortions provoked by the difference in the ionic radii of Al^{3+}/In^{3+} compared to that of Zn^{2+} (the radii of Al^{3+}/In^{3+} ions is smaller than that of Zn^{2+}). Furthermore, we remark that any characteristic diffraction peaks of Al_2O_3 or zinc spinel ($ZnAl_2O_4$) and In_2O_3 phases in the AZO and IZO thin films' diffraction patterns are presented, indicating that Al^{3+} or In^{3+} ions are substituted into Zn^{2+} ion sites. Hence, we conclude that the presence of Al or In atoms does not change the crystal structure of ZnO film in small concentrations. Other researchers' groups have also reported similar observations [38–41].

The mean crystallite size can be estimated according to the Debye–Scherrer formula below by applying the integral width β of the (002) line:

$$D = \frac{k \times \lambda}{\beta \times cos\theta} \tag{1}$$

where D represents the mean crystallite size, k corresponds to the shape factor (0.94), λ indicates the wavelength of the incident X-ray (1.5406Å), β implies the full width at half maximum (FWHM) of the (002) peak in radians, and θ is the Bragg's angle in degrees.

The dislocation density of the films (δ) is designated by the equation $\delta = \frac{1}{D^2}$. It is known that grain boundaries and other dislocations decelerate the dislocation in the stage of polycrystal materials' deformation [7]. The dislocation density and crystallite size possess an inverse link that could be correlated to mechanical properties, supported by comparing the results in Table 1 of dislocation density to crystallite size. These results highlight that a decrease in crystallite size will increase the dislocation density.

Table 1. Variation in the Bragg's angle 2θ; the full width at half maximum; the crystallite size; lattice parameter c; main strain ε; and the stress of undoped ZnO, AZO, and IZO thin films.

Sample	(002) Peak Angle (2θ)	FWHM of (002) Peak (°)	Crystallite Size (nm)	Dislocation Density (10^{14} Lines/m²)	Lattice Parameter c (Å)	Strain of c-axis (%)	Stress (GPa)
ZnO	34.392	0.317	27.35	13.37	5.210	0.07	−16.36
AZO 1%	34.457	0.373	23.26	18.48	5.202	−0.1	22.58
AZO 3%	34.372	0.485	17.90	31.21	5.214	0.14	−33.04
AZO 5%	34.338	0.787	11.04	82.05	5.219	0.24	−55.4
IZO 1%	34.406	0.420	20.67	23.41	5.209	0.05	−10.78
IZO 3%	34.279	0.618	14.05	50.66	5.228	0.41	−94.62
IZO 5%	34.355	1.733	5.01	39.84	5.216	0.19	−44.27

The c-axis strain (ε_{zz}) values were estimated from the observed shift in the diffraction peak between their position in the XRD spectra via the formula $\varepsilon_{zz} = \frac{c-c_0}{c_0} \times 100\%$ [42], where c denotes the lattice parameter of the strained films calculated from the X-ray diffraction data, whilst c_0 is the unstrained lattice parameter of bulk ZnO (c_0 = 5.20662Å) [43]. The c-lattice parameter in this work was calculated according to the formula $c = \lambda / \sin\theta$, Bragg's law for hexagonal crystals.

For hexagonal crystal structure, the residual stress (σ) in the plane of the film can be calculated using the biaxial strain model in the equation below:

$$\sigma = \frac{2c_{13}^2 - c_{33}(c_{11} + c_{12})}{2c_{13}} \times \varepsilon_{zz} \tag{2}$$

where c_{ij} represents the elastic stiffness constants (i.e., c_{11} = 208.8 GPa, c_{12} = 119.7 GPa, c_{13} = 104.2 GPa, and c_{33} = 213.8 GPa) [44]. Substituting these values in the above equation gives $\sigma = -233 \times \varepsilon_{zz}$ GPa.

The Bragg's angle (2θ); the FWHM; the average crystallite size; the lattice parameter c; the main strain ε; and the stress of undoped ZnO, AZO, and IZO thin films are presented in Table 1. It is found that, upon doping with aluminum or indium, there is a gradual decrease in crystallite size, which is more pronounced for In. There are similar results showing that the increase in the Al doping level up to 2% deteriorates the films' crystallinity, primarily because of Al segregation at grain boundaries. Moreover, the ions of Al^{3+} and In^{3+} have a larger nuclear charge than the Zn^{2+} ion, capturing a greater extent of oxygen, and this may be another parameter that affects the crystallinity [1].

In the case of ZnO doping with Al, we do not observe significant changes in the c lattice parameter because the ionic radius of aluminum (0.56 Å) is smaller than that of zinc (0.74 Å). For the same reason, at low doping concentrations, the residual stress is similar to that of pure ZnO. A slight increase in the *c* lattice parameter is observed for Al doping with concentrations larger than 1%. This is because some aluminum ions may occupy interstitial positions in the ZnO lattice [1]. In the case of In doping, the lattice constant of IZO is also larger than that of pure ZnO films [45], because the bigger In^{3+} ions (radius 0.84 Å) substitute the Zn^{2+} ions (radius 0.74 Å) in the lattice. For this reason and for In doping larger than 1%, the lattice is distorted, and the residual stress is increased. The minus sign indicates that the residual stress is compressive. This results in a smaller crystallite size for both dopants.

As the FWHM values in Table 1 result from the XRD measurements in Figure 3, they further support the above discussion. For all three concentration values of both dopants, the FWHM values increase monotonically with concentration; furthermore, the FWHM values of In are larger than those of Al. This results in a decrease in the crystalline size, in particular, a stronger decrease for In, as clearly derived from Equation (1).
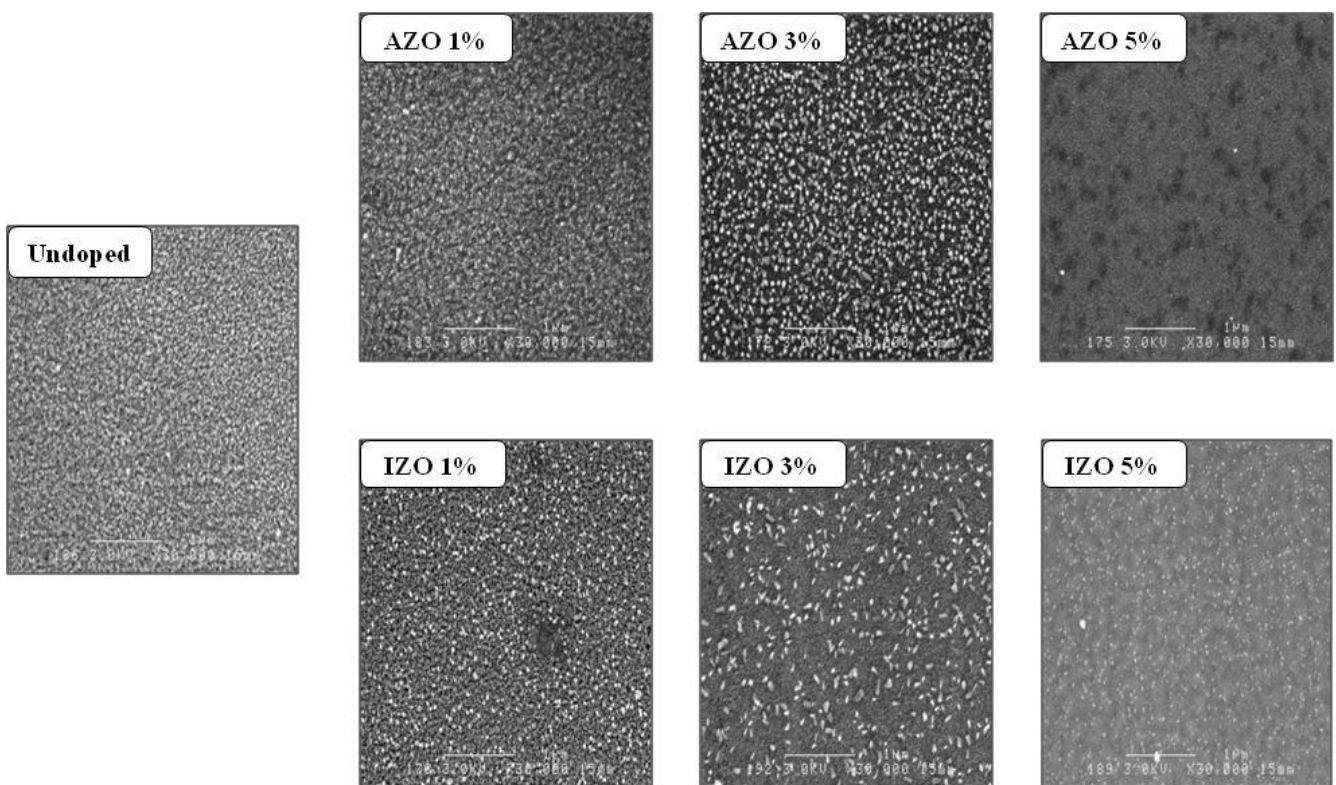

Figure 3. SEM micrographs of undoped ZnO, AZO, and IZO thin films deposited at various doping concentrations.

3.2. Surface Morphology Analysis

SEM and AFM images of the prepared ZnO, AZO, and IZO thin films are shown in Figures 3 and 4, respectively. The SEM images reveal that each film consists of a homogeneous distribution of grains that are randomly oriented, corroborating the polycrystalline structure confirmed by XRD analysis. However, it is evident that there is a remarkable change in the morphology of the films, which correlates with the type of dopant and doping concentration. No film cracking is observed. Furthermore, we notice that, at the 1% doping level, the surface appears almost the same as the surface of pure ZnO, which is granular, highly dense, and compact, though it exhibits a more porous structure. This ZnO microstructure is coherent with a nanocrystalline structure with its distinct outlines of grains suggested by XRD analysis. The surface of the 3% AZO thin film presents a structure with irregular and disordered grains. In contrast, the corresponding IZO film consists of particles forming a uniform background layer on which particles with sizes of a few hundred nanometers are evenly distributed. In both cases, this explains the poor crystallinity that the XRD patterns present. For the 5% doping concentration, the surfaces of both AZO and IZO thin films change entirely compared to the lower concentration values, clearly showing the influence of the incorporation of dopants at high concentrations on the morphology of the undoped ZnO films. The AZO film shows a smoother surface with some pores of a few hundred nanometers in size. In particular, the SEM micrograph of IZO 3% (Figure 3) comprises "rice-like" grains, with sizes of several tens of nanometers.
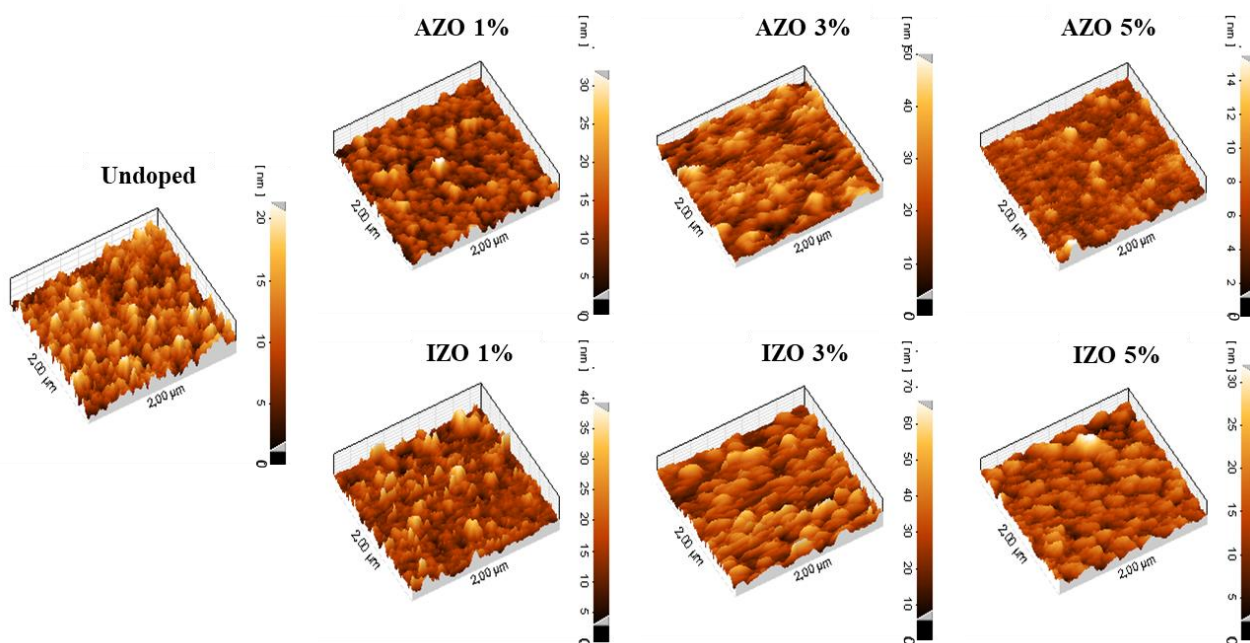

Figure 4. Three-dimensional AFM images of undoped ZnO, AZO, and IZO thin films deposited at various doping concentrations.

Several authors have reported similar network textures of undoped [46–48] and Al-doped [47,49] ZnO films prepared by applying the same deposition technique. In the literature, several groups argued that the growth of the film along the *c*-axis orientation deteriorates due to the formation of surface wrinkles [46], and some others have observed that the evolution of the surface texturing is strongly affected by the heating procedure [48]. Network thin films of Ni-doped ZnO have been grown with the same solution type used in this work, and it was noticed that an increase in the Ni doping concentration led to a decrease in the network density [47]. This phenomenon was also observed for thin films prepared by applying two different compositions of AZO solutions [49]. According to Ref. [50], "*the formation of a continuous network is ascribed to the competition between sintering*

and crystallization, i.e., the densification of the amorphous matrix is arrested when a certain fraction of crystallinity develops". Based on the above discussion, we conclude that several factors, including sol composition, doping concentration, and heat treatment, should act in combination to guide the network texture's self-assembly. Among them, heat treatment is of primary importance [49].

In the three-dimensional AFM (contact mode) images (see Figure 4), we observe that the surfaces of all films with different compositions are very smooth and exhibit hillock morphology. Both doped and undoped thin films include columnar grains growing along the c-axis, perpendicular to the substrate surface, which is in agreement with the XRD results. The grain boundaries of ZnO are clear, and the grains seem to have similar dimensions and a round shape in the plane. The evidence of crystallization is mainly due to the vertical growth of the grains. The insertion of Al or In dopants affects the normal growth of ZnO crystals, and as we can observe, it changes the surface morphology, resulting in fewer grains with smaller sizes. These effects increase with the concentration of the dopants. Moreover, for both AZO and IZO and for the 3% and 5% dopant concentrations, we observe that the grain boundaries are unclear, and the surface morphology, which refers to the grain growth mode, changes completely. This may be an effect of increasing the film thickness while increasing the dopant concentration. The effect of the film thickness of sol–gel dip-coated ZnO [36] and PLD-grown AZO [51] on the structural properties has shown that the grains' growth mode turns from vertical to lateral for thicker films. This result seems to be independent of the growth process.

The degree of surface roughness was deduced from AFM studies by determining the average and root mean square (rms) values, and the values confirm that the surfaces of all thin films are very smooth. As denoted in Table 2, the roughness increases for the 1% doping concentration regardless of the dopant, and it gradually reduces by increasing the concentration of Al or In.

Table 2. Average and root mean square (rms) values of surface roughness measured using AFM.

Sample	R_a (nm)	R_{rms} (nm)
ZnO (reference)	3.38	4.23
AZO 1%	4.44	5.76
AZO 3%	3.17	4.19
AZO 5%	1.45	2.11
IZO 1%	5.08	6.56
IZO 3%	4.57	5.82
IZO 5%	2.82	3.57

3.3. Optical Properties

The effects of the dopant type and concentration on the optical transmittance and the bandgap for the sol–gel-grown ZnO, AZO, and IZO thin films after thermal annealing were investigated. In Figure 5, it is evident that all thin films exhibit high transmittance in the visible NIR region from 82% to 94%, opening up possibilities for usage in optoelectronic devices as transparent windows. The high transmittance level is enhanced by the fact that all thin films are oriented along the *c*-axis (002) plane because it avoids light scattering at the grain boundaries.

All thin films present a sharp absorption edge near the ultraviolet region at about 380 nm, which corresponds to ZnO's optical bandgap transition. In addition, the weak modulation in the spectra is due to interference effects between the film surface and the film/surface interface.
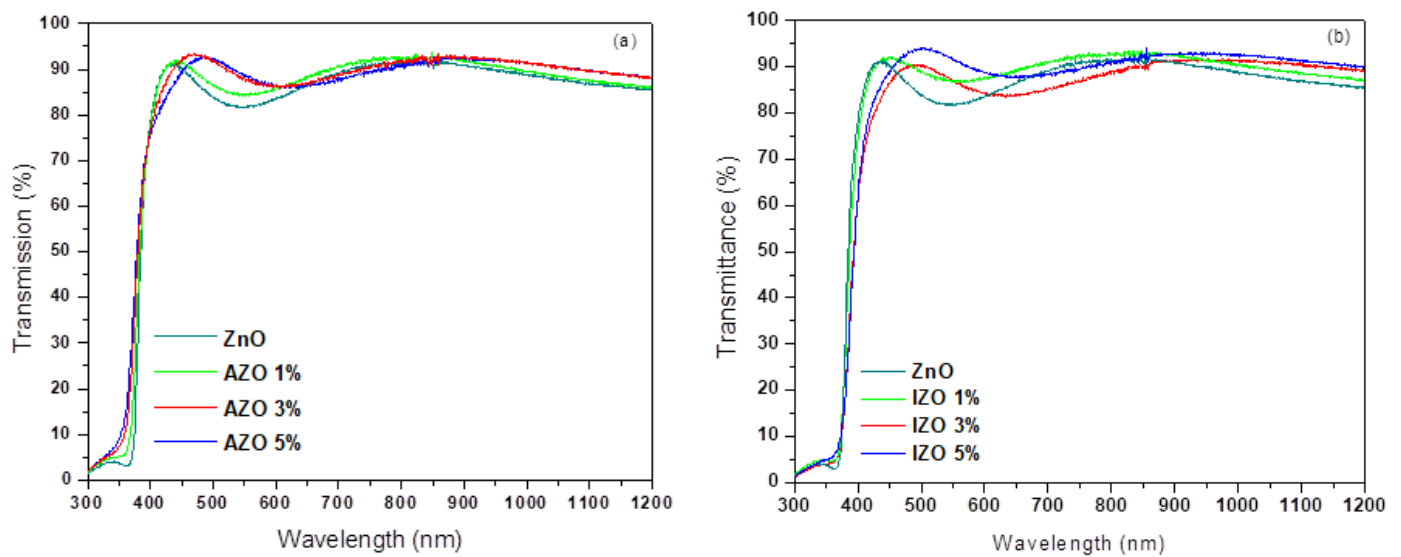
Figure 5. Optical transmittance spectra of undoped ZnO, (**a**) AZO, and (**b**) IZO thin films.

The optical bandgap of the thin films was estimated by employing the Tauc model [52] taking into account that ZnO is a direct transition semiconductor material following from the international literature:

$$(ahv) = A(hv - E_g)^{1/2} \tag{3}$$

where α indicates the absorption coefficient, hv denotes the photon energy, and A corresponds to a constant that depends on the electron–hole mobility. E_g is the optical bandgap, derived by extrapolating the linear section of the plot of $(\alpha hv)^2$ versus photon energy (x-axis). The acquired E_g values of the films are presented in Table 3 and Figure 6. Although the optical bandgap of the AZO thin films increases monotonically while increasing the Al concentration, the bandgap of the IZO films also decreases monotonically while increasing the In concentration. In a previous publication [37], we deposited ZnO, AZO, and IZO thin films and found similar results: the bandgap of the AZO films increased with the Al concentration, while the IZO bandgap decreased with the In concentration. Those films were deposited using a dual-target, dual-laser PLD, and the dopant concentration was defined by the laser fluence.

Table 3. The thickness and the calculated energy gap of undoped ZnO, AZO, and IZO thin films.

Sample	Thickness (nm)	Eg (eV)
ZnO (reference)	234	3.26
AZO 1%	244	3.28
AZO 3%	247	3.29
AZO 5%	261	3.30
IZO 1%	245	3.24
IZO 3%	270	3.22
IZO 5%	289	3.19

In the case of Al doping, the value of the bandgap energy demonstrates an increase from 3.26 to 3.30 eV with augmentation of the doping concentration. This increase can be elucidated by the Burstein–Moss theory: the phenomenon of the energy band widening (blue shift) arises from the shift of the Fermi plane to the conduction band of the degenerate semiconductor [53,54].

By increasing the doping concentration, the donor electrons fill the energy states above and close the bottom of the semiconductor's conduction band. Taking into account the Pauli exclusion principle, these states can be occupied by only one (donor) electron. Therefore,

for electrons from the valence band, the optical vertical transitions (see Equation (2)) need a photon with more energy than that for the undoped ZnO [55]. Based on all of the above, we conclude that the experimentally measured energy gap resulting from the transmittance and reflectance spectra is greater than the "real" one specified by the semiconductor lattice structure. This phenomenon has been observed not only in the case of Al doping [56] but also with the B and Ga doping of ZnO [55,57].
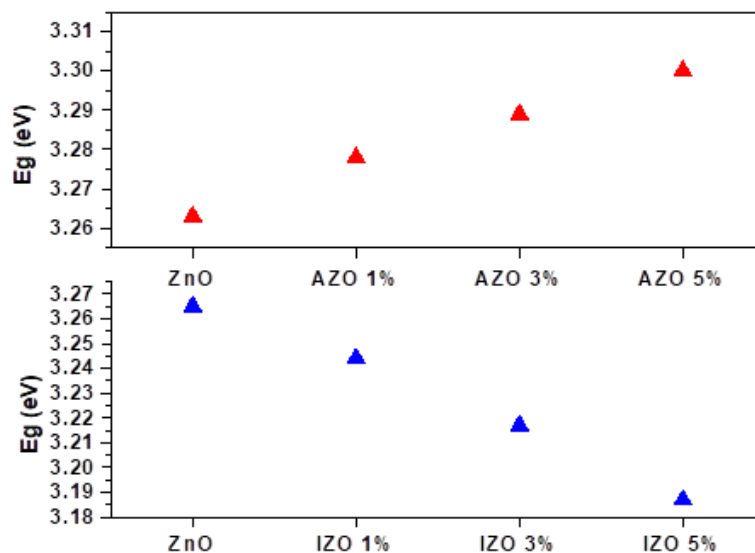

Figure 6. The energy gap of undoped ZnO, AZO, and IZO thin films deposited at various doping concentrations.

Obviously, increasing the content of external contaminants cannot continue indefinitely. Furthermore, the Burnstein–Moss effect cannot explain the decrease in E_g in the In:ZnO films in this work. A reduction in E_g [58] on amorphous Si and Ge has previously been observed, and it was attributed to the existence of energy states (the so-called Urbach tails [59]) extending into the energy gap just above the valence band. Such states are due to the deviation of amorphous Si and Ge from the periodicity of the monocrystal. As shown in Figure 7, the energy states of the valence band extend to higher states and those of the conduction band to lower states inside the energy gap of E_v–E_c as it is defined by a single crystal material. This results in new electron excitations that become possible between the valence band and the Urbach states, between the Urbach states and the conduction band, and also between the Urbach states themselves. The energy gap resulting from the absorption spectra appears shrunken, and the width of the Urbach states becomes larger as the lattice disorder increases due to various causes, including doping. In conclusion, the widening of E_g due to the Burnstein–Moss phenomenon and the shrinkage as a result of lattice disorders act competitively, and one of the two prevail as appropriate.

In this work, the In-doped thin films exhibit different behavior, and the narrowing of the energy bandgap with the incorporation of In has been reported in many articles in the literature [60–63]. Moreover, the results show that the behaviors of the In-doped films are independent of the way in which they are developed (e.g., spin coating and thermal evaporation). A more in-depth understanding of the decrease in E_g is reported in the works of Tang et al. [64] and Saha et al. [65]. Tang et al. deposited In:ZnO thin films by applying the MOCVD technique. They calculated the electron density N_e as a function of the In concentration and showed that, for values less than $10^{19}/cm^3$, E_g remains constant, while for values ~$10^{20}/cm^3$ and above, they observed a reduction in E_g (critical concentration by Mott). Similarly, Saha et al. developed thin films of Ga:ZnO using the sol–gel technique, and E_g was measured as a function of the Ga concentration. It was found

that E_g increased for low Ga concentration values (Burnstein–Moss effect), while for higher values, it decreased.
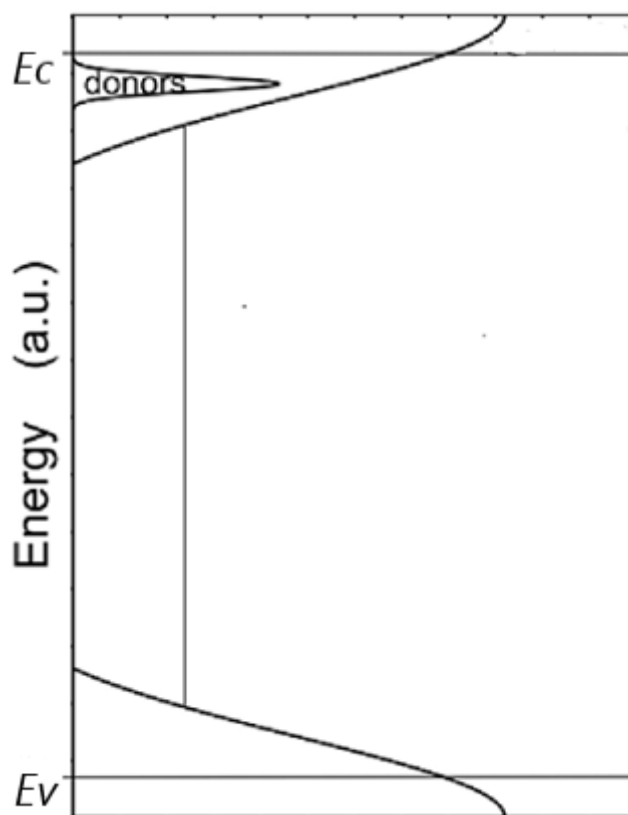

Figure 7. Schematic representation of an n-type semiconductor with valence band (E_v) and conduction band (E_c), and the donor states and the Urbach states in the energy gap.

Our explanation of all of the above is as follows: The elements used as dopants of ZnO are those of the third group of the periodic table, namely, boron (B), aluminum (Al), gallium (Ga), and indium (In). These elements initially replace the Zn^{2+} in lattice positions, and by increasing the concentration, they occupy interstitial positions as neutral atoms or ions. As we can observe from Table 4, because of its size, even at relatively low concentrations, In leads to such a disorder in the ZnO lattice as to create Urbach states and provoke the reduction in E_g [64]. The case for Ga:ZnO [65] is more characteristic; the Ga concentrations that were applied show a transition from the Burnstein–Moss area (increase in E_g) to the Urbach area (decrease in E_g). It is obvious that the use of the elements B and Al causes a negligible disorder due to their small ionic radius and that E_g increased (Burnstein–Moss area).

Table 4. The ionic radius of Zn^{2+} and of its doping elements.

M:ZnO	ZnO	B:ZnO	Al:ZnO	Ga:ZnO	In:ZnO
R_i^{3+}(M) pm	88	41	68	76	94

3.4. Electrical Properties

The surface sheet resistance Rs and the electrical resistivity ρ of the thin films were measured at room temperature by applying the method of Van der Pauw. It was found that the specific electrical resistance is highly dependent on the type of the doping element and its concentration in the ZnO lattice. As we can observe from Table 5, for a doping concentration of 1% for both Al and In, the resistivity initially decreases by about 20 times compared

with that of ZnO, while by further increasing the dopants, we notice a gradual increase again. Despite the different deposition techniques, this dependence of the resistivity on the doping concentration has also been observed in the literature [60,66].

Table 5. The thickness and the calculated sheet resistance and electrical resistivity of undoped ZnO, AZO, and IZO thin films.

Sample	Thickness (nm)	Sheet Resistance Rs (MΩ)	Electrical Resistivity ρ (Ωcm)
ZnO (reference)	234	69.47	1625.60
AZO 1%	244	2.35	57.34
AZO 3%	247	5.67	140.05
AZO 5%	261	14.06	366.96
IZO 1%	245	3.51	85.99
IZO 3%	270	6.91	186.57
IZO 5%	289	6.09	176

Electrical resistivity is closely related to the carrier density of electrons N_e and the mobility μ_e by the relationship $1/\rho = e\, N_e\, \mu_e$, where e is the charge of an electron $(1.60 \times 10^{-19}$ C) [67]. The carrier density depends on the dopant concentration, while the mobility is determined by the scattering of electrons, which is related to the crystal structure of the material. In the literature, N_e and μ_e were measured independently for IZO [64] and AZO [66] thin films, and it was found that N_e systematically increased with the increase in doping content, which is also expected in the present study.

However, the dopant concentration affects the mobility in two ways: (1) As is also stated in Kim et al. [66], a reduction in the mobility μ_e occurs due to the fact that, with an increase in dopants, Al^{3+} and In^{3+} ions substitute at Zn^{2+} cation sites or are incorporated in interstitial positions that deteriorate the periodicity of the ZnO lattice and scatter the donor electrons. In Table 1, we can observe that, for the 3% and 5% dopant concentrations, the *c*-axis lattice parameter is larger than that of ZnO, which is an indication of the existence of Al^{3+} and In^{3+} ions in interstitial positions (2). In the present work, as well as in Ref [66], there is a noticeable grain size reduction when increasing the content of the dopants (see Table 1). This entails an increased number of grain boundaries that form electron scattering regions, which contribute to a further reduction in mobility. As the electrical resistivity is given by the product $N_e\, \mu_e$, the value of ρ is defined by the interplay between the increase in N_e and the decrease in μ_e, as well as the rate of their increase and decrease when the doping concentration changes. It is also well known that, the bigger the grains, the lesser the grain boundaries (see Figure 4). When the number of grain boundaries, which act as a barrier to electron propagation, in the thin film reduce, as observed with the thin films deposited at higher temperatures (500 °C annealing temperature), the resistivity lowers since it increases the mean free path for the electrons. This works in favor of the sensor performance.

4. Conclusions

We successfully fabricated high-quality ZnO, AZO, and IZO thin films via the sol–gel spin coating technique. This work constitutes a comprehensive analysis of ZnO structures, which may be potentially applied in optoelectronics and sensing applications. The core of the present research was a comparison of the structural, morphological, optical, and electrical parameters between undoped ZnO and IZO and AZO polycrystalline films in the 234–289 nm thickness range. The increase in the dopant concentration decreased the crystallinity of the AZO and IZO thin films. The optical transmittance spectra of the films showed a high transmittance value of over 90% in the visible range, making the films suitable for use in optoelectronic devices. The optical bandgap energy *Eg* increased for AZO and decreased for IZO while increasing the dopant concentration. The electrical resistivity decreased significantly with doping, and it increased slightly with the type and dopant concentration.

References

1. Salam, S.; Islam, M.; Akram, A. Sol-gel synthesis of intrinsic and aluminum-doped zinc oxide thin films as transparent conducting oxides for thin film solar cells. *Thin Solid Films* **2013**, *529*, 242–247. [CrossRef]
2. Choi, Y.S.; Kang, J.W.; Hwang, D.K.; Park, S.J. Recent advances in ZnO-based light-emitting diodes. *IEEE Trans. Electron Devices* **2010**, *57*, 26–41. [CrossRef]
3. Sarma, B.; Barman, D.; Sarma, B.K. AZO (Al:ZnO) thin films with high figure of merit as stable indium free transparent conducting oxide. *Appl. Surf. Sci.* **2019**, *479*, 786–795. [CrossRef]
4. Rahman, F. Zinc oxide light-emitting diodes: A review. *Opt. Eng.* **2019**, *58*, 1. [CrossRef]
5. Ding, M.; Guo, Z.; Zhou, L.; Fang, X.; Zhang, L.; Zeng, L.; Xie, L.; Zhao, H. One-dimensional zinc oxide nanomaterials for application in high-performance advanced optoelectronic devices. *Crystals* **2018**, *8*, 223. [CrossRef]
6. Baskoutas, S. Special issue: Zinc oxide nanostructures: Synthesis and characterization. *Materials* **2018**, *11*, 873. [CrossRef]
7. Fiat Varol, S.; Babür, G.; Çankaya, G.; Kölemen, U. Synthesis of sol-gel derived nano-crystalline ZnO thin films as TCO window layer: Effect of sol aging and boron. *RSC Adv.* **2014**, *4*, 56645–56653. [CrossRef]
8. Ocola, L.E.; Wang, Y.; Divan, R.; Chen, J. Multifunctional UV and gas sensors based on vertically nanostructured zinc oxide: Volume versus surface effect. *Sensors* **2019**, *19*, 2061. [CrossRef]
9. Regmi, G.; Rohini, M.; Reyes-Figueroa, P.; Maldonado, A.; de la Luz Olvera, M.; Velumani, S. Deposition and characterization of ultrathin intrinsic zinc oxide (i-ZnO) films by radio frequency (RF) sputtering for propane gas sensing application. *J. Mater. Sci. Mater. Electron.* **2018**, *29*, 15682–15692. [CrossRef]
10. Lee, J.; Seul, H.; Jeong, J.K. Solution-processed ternary alloy aluminum yttrium oxide dielectric for high performance indium zinc oxide thin-film transistors. *J. Alloys Compd.* **2018**, *741*, 1021–1029. [CrossRef]
11. Gu, P.; Zhu, X.; Yang, D. Effect of annealing temperature on the performance of photoconductive ultraviolet detectors based on ZnO thin films. *Appl. Phys. A Mater. Sci. Process.* **2019**, *125*, 50. [CrossRef]
12. Li, Y.; Feng, J.; Zhang, J.; He, B.; Wu, Y.; Zhao, Y.; Xu, C.; Wang, J. Towards high-performance linear piezoelectrics: Enhancing the piezoelectric response of zinc oxide thin films through epitaxial growth on flexible substrates. *Appl. Surf. Sci.* **2021**, *556*, 149798. [CrossRef]
13. Laurenti, M.; Cauda, V. Porous zinc oxide thin films: Synthesis approaches and applications. *Coatings* **2018**, *8*, 67. [CrossRef]
14. Tsoutsouva, M.G.; Panagopoulos, C.N.; Kompitsas, M. Laser energy density, structure and properties of pulsed-laser deposited zinc oxide films. *Appl. Surf. Sci.* **2011**, *257*, 6314–6319. [CrossRef]
15. Özgür, Ü.; Avrutin, V.; Morkoç, H. Zinc Oxide Materials and Devices Grown by Molecular Beam Epitaxy. In *Molecular Beam Epitaxy*; Elsevier: Amsterdam, The Netherlands, 2018; pp. 343–375. ISBN 9780128121368.
16. Yin, J.; Gao, F.; Wei, C.; Lu, Q. Water Amount Dependence on Morphologies and Properties of ZnO nanostructures in Double-solvent System. *Sci. Rep.* **2014**, *4*, 3736. [CrossRef]
17. Xu, L.; Zheng, G.; Miao, J.; Xian, F. Dependence of structural and optical properties of sol-gel derived ZnO thin films on sol concentration. *Appl. Surf. Sci.* **2012**, *258*, 7760–7765. [CrossRef]
18. Lee, C.Y.; Kuo, Y.P.; Chen, P.Y.; Lu, H.H.; Lin, M.Y. Influence of annealing temperature on weak-cavity top-emission red quantum dot light emitting diode. *Nanomaterials* **2019**, *9*, 1639. [CrossRef]
19. Yu, S.; Li, L.; Lyu, X.; Zhang, W. Preparation and investigation of nano-thick FTO/Ag/FTO multilayer transparent electrodes with high figure of merit. *Sci. Rep.* **2016**, *6*, 20399. [CrossRef]
20. Wang, W.; Peng, H.; Chen, S. Highly transparent quantum-dot light-emitting diodes with sputtered indium-tin-oxide electrodes. *J. Mater. Chem. C* **2016**, *4*, 1838–1841. [CrossRef]

21. Chichibu, S.F.; Shima, K.; Kojima, K.; Takashima, S.; Edo, M.; Ueno, K.; Ishibashi, S.; Uedono, A. Large electron capture-cross-section of the major nonradiative recombination centers in Mg-doped GaN epilayers grown on a GaN substrate. *Appl. Phys. Lett.* **2018**, *112*, 211901. [CrossRef]

22. Ying, Z.; Zhu, Y.; Feng, X.; Xiu, J.; Zhang, R.; Ma, X.; Deng, Y.; Pan, H.; He, Z. Sputtered Indium-Zinc Oxide for Buffer Layer Free Semitransparent Perovskite Photovoltaic Devices in Perovskite/Silicon 4T-Tandem Solar Cells. *Adv. Mater. Interfaces* **2021**, *8*, 2170029. [CrossRef]

23. Sanchez-Sobrado, O.; Mendes, M.J.; Mateus, T.; Costa, J.; Nunes, D.; Aguas, H.; Fortunato, E.; Martins, R. Photonic-structured TCO front contacts yielding optical and electrically enhanced thin-film solar cells. *Sol. Energy* **2020**, *196*, 92–98. [CrossRef]

24. Lai, F.I.; Hsieh, M.Y.; Yang, J.F.; Hsu, Y.C.; Kuo, S.Y. Antireflection layer of ZnO nanorod embedded in PDMS film for enhancing omnidirectional photovoltaic performance of CIGS photovoltaic cell. *Int. J. Energy Res.* **2021**, *45*, 1142–1149. [CrossRef]

25. Jošt, M.; Köhnen, E.; Morales-Vilches, A.B.; Lipovšek, B.; Jäger, K.; Macco, B.; Al-Ashouri, A.; Krč, J.; Korte, L.; Rech, B.; et al. Textured interfaces in monolithic perovskite/silicon tandem solar cells: Advanced light management for improved efficiency and energy yield. *Energy Environ. Sci.* **2018**, *11*, 3511–3523. [CrossRef]

26. Kranz, L.; Abate, A.; Feurer, T.; Fu, F.; Avancini, E.; Löckinger, J.; Reinhard, P.; Zakeeruddin, S.M.; Grätzel, M.; Buecheler, S.; et al. High-efficiency polycrystalline thin film tandem solar cells. *J. Phys. Chem. Lett.* **2015**, *6*, 2676–2681. [CrossRef]

27. Hjiri, M.; Zahmouli, N.; Dhahri, R.; Leonardi, S.G.; El Mir, L.; Neri, G. Doped-ZnO nanoparticles for selective gas sensors. *J. Mater. Sci. Mater. Electron.* **2017**, *28*, 9667–9674. [CrossRef]

28. Nimbalkar, A.R.; Patil, N.B.; Ganbavle, V.V.; Mohite, S.V.; Madhale, K.V.; Patil, M.G. Sol-gel derived aluminium doped zinc oxide thin films: A view of aluminium doping effect on physicochemical and NO$_2$ sensing properties. *J. Alloys Compd.* **2019**, *775*, 466–473. [CrossRef]

29. Khorramshahi, V.; Karamdel, J.; Yousefi, R. Acetic acid sensing of Mg-doped ZnO thin films fabricated by the sol–gel method. *J. Mater. Sci. Mater. Electron.* **2018**, *29*, 14679–14688. [CrossRef]

30. Hjiri, M.; Dhahri, R.; El Mir, L.; Bonavita, A.; Donato, N.; Leonardi, S.G.; Neri, G. CO sensing properties of Ga-doped ZnO prepared by sol-gel route. *J. Alloys Compd.* **2015**, *634*, 187–192. [CrossRef]

31. Navale, S.C.; Ravi, V.; Mulla, I.S.; Gosavi, S.W.; Kulkarni, S.K. Low temperature synthesis and NOx sensing properties of nanostructured Al-doped ZnO. *Sens. Actuators B Chem.* **2007**, *126*, 382–386. [CrossRef]

32. Chaabouni, F.; Abaab, M.; Rezig, B. Metrological characteristics of ZNO oxygen sensor at room temperature. *Sens. Actuators B Chem.* **2004**, *100*, 200–204. [CrossRef]

33. Koshizaki, N.; Oyama, T. Sensing characteristics of ZnO-based NOx sensor. *Sens. Actuators B Chem.* **2000**, *66*, 119–121. [CrossRef]

34. Bharath, S.P.; Bangera, K.V.; Shivakumar, G.K. Enhanced gas sensing properties of indium doped ZnO thin films. *Superlattices Microstruct.* **2018**, *124*, 72–78. [CrossRef]

35. Znaidi, L. Sol-gel-deposited ZnO thin films: A review. *Mater. Sci. Eng. B Solid-State Mater. Adv. Technol.* **2010**, *174*, 18–30. [CrossRef]

36. Xu, L.; Li, X.; Chen, Y.; Xu, F. Structural and optical properties of ZnO thin films prepared by sol-gel method with different thickness. *Appl. Surf. Sci.* **2011**, *257*, 4031–4037. [CrossRef]

37. Girtan, M.; Kompitsas, M.; Mallet, R.; Fasaki, I. On physical properties of undoped and Al and In doped zinc oxide films deposited on PET substrates by reactive pulsed laser deposition. *Eur. Phys. J. Appl. Phys.* **2010**, *51*, 33212. [CrossRef]

38. Quang, L.H.; Swee Kuan, L.; Kia Liang, G.G. Structural and electrical properties of single crystal indium doped ZnO films synthesized by low temperature solution method. *J. Cryst. Growth* **2010**, *312*, 437–442. [CrossRef]

39. Ilican, S.; Caglar, Y.; Caglar, M.; Yakuphanoglu, F. Electrical conductivity, optical and structural properties of indium-doped ZnO nanofiber thin film deposited by spray pyrolysis method. *Phys. E Low-Dimens. Syst. Nanostruct.* **2006**, *35*, 131–138. [CrossRef]

40. Kumar, P.M.R.; Kartha, C.S.; Vijayakumar, K.P.; Abe, T.; Kashiwaba, Y.; Singh, F.; Avasthi, D.K. On the properties of indium doped ZnO thin films. *Semicond. Sci. Technol.* **2005**, *20*, 120–126. [CrossRef]

41. Dhamodharan, P.; Chen, J.; Manoharan, C. Fabrication of In doped ZnO thin films by spray pyrolysis as photoanode in DSSCs. *Surf. Interfaces* **2021**, *23*, 100965. [CrossRef]

42. Malek, M.F.; Mamat, M.H.; Khusaimi, Z.; Sahdan, M.Z.; Musa, M.Z.; Zainun, A.R.; Suriani, A.B.; Sin, N.D.M.; Hamid, S.B.A.; Rusop, M. Sonicated sol-gel preparation of nanoparticulate ZnO thin films with various deposition speeds: The highly preferred c-axis (002) orientation enhances the final properties. *J. Alloys Compd.* **2014**, *582*, 12–21. [CrossRef]

43. Abrahams, S.C.; Bernstein, J.L. Remeasurement of the structure of hexagonal ZnO. *Acta Crystallogr. Sect. B Struct. Crystallogr. Cryst. Chem.* **1969**, *25*, 1233–1236. [CrossRef]

44. Wang, Y.G.; Lau, S.P.; Lee, H.W.; Yu, S.F.; Tay, B.K.; Zhang, X.H.; Tse, K.Y.; Hng, H.H. Comprehensive study of ZnO films prepared by filtered cathodic vacuum arc at room temperature. *J. Appl. Phys.* **2003**, *94*, 1597–1604. [CrossRef]

45. Chen, K.J.; Hung, F.Y.; Chang, S.J.; Hu, Z.S. Microstructures, optical and electrical properties of In-doped ZnO thin films prepared by sol-gel method. *Appl. Surf. Sci.* **2009**, *255*, 6308–6312. [CrossRef]

46. Miller, J.B.; Hsieh, H.J.; Howard, B.H.; Broitman, E. Microstructural evolution of sol-gel derived ZnO thin films. *Thin Solid Films* **2010**, *518*, 6792–6798. [CrossRef]

47. Tsay, C.Y.; Fan, K.S.; Chen, S.H.; Tsai, C.H. Preparation and characterization of ZnO transparent semiconductor thin films by sol-gel method. *J. Alloys Compd.* **2010**, *495*, 126–130. [CrossRef]

48. Farag, A.A.M.; Cavas, M.; Yakuphanoglu, F.; Amanullah, F.M. Photoluminescence and optical properties of nanostructure Ni doped ZnO thin films prepared by sol-gel spin coating technique. *J. Alloys Compd.* **2011**, *509*, 7900–7908. [CrossRef]

49. Wang, M.; Liang, W.; Yang, Y.; Yang, J.; Cheng, X.; Hahn, S.H.; Kim, E.J. Sol-gel derived transparent conducting ZnO:Al thin films: Effect of crystallite orientation on conductivity and self-assembled network texture. *Mater. Chem. Phys.* **2012**, *134*, 845–850. [CrossRef]

50. Scherer, G.W. Sintering of Sol-Gel Films. *J. Sol-Gel Sci. Technol.* **1997**, *8*, 353–363. [CrossRef]

51. Dong, B.Z.; Fang, G.J.; Wang, J.F.; Guan, W.J.; Zhao, X.Z. Effect of thickness on structural, electrical, and optical properties of ZnO: Al films deposited by pulsed laser deposition. *J. Appl. Phys.* **2007**, *101*, 033713. [CrossRef]

52. Tauc, J. *Optical Properties of Amorphous Semiconductors*; Springer: Boston, MA, USA, 1974; ISBN 9781467344791.

53. Burstein, E. Anomalous optical absorption limit in InSb. *Phys. Rev.* **1954**, *93*, 632–633. [CrossRef]

54. Di Trolio, A.; Bauer, E.M.; Scavia, G.; Veroli, C. Blueshift of optical band gap in c-axis oriented and conducting Al-doped ZnO thin films. *J. Appl. Phys.* **2009**, *105*, 113109. [CrossRef]

55. Kumar, V.; Singh, R.G.; Purohit, L.P.; Mehra, R.M. Structural, Transport and Optical Properties of Boron-doped Zinc Oxide Nanocrystalline. *J. Mater. Sci. Technol.* **2011**, *27*, 481–488. [CrossRef]

56. Al Farsi, B.; Souier, T.M.; Al Marzouqi, F.; Al Maashani, M.; Bououdina, M.; Widatallah, H.M.; Al Abri, M. Structural and optical properties of visible active photocatalytic Al doped ZnO nanostructured thin films prepared by dip coating. *Opt. Mater.* **2021**, *113*, 110868. [CrossRef]

57. Babar, A.R.; Deshamukh, P.R.; Deokate, R.J.; Haranath, D.; Bhosale, C.H.; Rajpure, K.Y. Gallium doping in transparent conductive ZnO thin films prepared by chemical spray pyrolysis. *J. Phys. D Appl. Phys.* **2008**, *41*, 135404. [CrossRef]

58. O'Leary, S.K.; Zukotynski, S.; Perz, J.M. Disorder and optical absorption in amorphous silicon and amorphous germanium. *J. Non. Cryst. Solids* **1997**, *210*, 249–253. [CrossRef]

59. Ayik, C.; Studenyak, I.; Kranjec, M.; Kurik, M. Urbach Rule in Solid State Physics. *Int. J. Opt. Appl.* **2014**, *4*, 76–83. [CrossRef]

60. Girtan, M.; Socol, M.; Pattier, B.; Sylla, M.; Stanculescu, A. On the structural, morphological, optical and electrical properties of sol-gel deposited ZnO:In films. *Thin Solid Films* **2010**, *519*, 573–577. [CrossRef]

61. Jie, J.; Wang, G.; Han, X.; Yu, Q.; Liao, Y.; Li, G.; Hou, J.G. Indium-doped zinc oxide nanobelts. *Chem. Phys. Lett.* **2004**, *387*, 466–470. [CrossRef]

62. Bae, S.Y.; Choi, H.C.; Na, C.W.; Park, J. Influence of in incorporation on the electronic structure of ZnO nanowires. *Appl. Phys. Lett.* **2005**, *86*, 1–3. [CrossRef]

63. Caglar, M.; Ilican, S.; Caglar, Y. Influence of dopant concentration on the optical properties of ZnO: In films by sol-gel method. *Thin Solid Films* **2009**, *517*, 5023–5028. [CrossRef]

64. Tang, K.; Gu, S.; Liu, J.; Ye, J.; Zhu, S.; Zheng, Y. Effects of indium doping on the crystallographic, morphological, electrical, and optical properties of highly crystalline ZnO films. *J. Alloys Compd.* **2015**, *653*, 643–648. [CrossRef]

65. Saha, M.; Ghosh, S.; Ashok, V.D.; De, S.K. Carrier concentration dependent optical and electrical properties of Ga doped ZnO hexagonal nanocrystals. *Phys. Chem. Chem. Phys.* **2015**, *17*, 16067–16079. [CrossRef] [PubMed]

66. Kim, H.; Piqué, A.; Horwitz, J.S.; Murata, H.; Kafafi, Z.H.; Gilmore, C.M.; Chrisey, D.B. Effect of aluminum doping on zinc oxide thin films grown by pulsed laser deposition for organic light-emitting devices. *Thin Solid Films* **2000**, *377–378*, 798–802. [CrossRef]

67. Schroder, D.K. *Semiconductor Material and Device Characterization*; John Wiley & Sons, Ltd.: New York, NY, USA, 1990.